Supporting Information

Ethylene Oligomerization Under Confinement Using Supported Cr(II) and Cr(III) Catalysts

Somnath Bhattacharya[a], Marc Högler[b], Johanna R. Bruckner[c], Boshra Atwi[a], Matthias Bauer[d], Niels Hansen[b], Felix R. Fischer[d], Michael R. Buchmeiser[a]**

[a]Institute of Polymer Chemistry, University of Stuttgart, Stuttgart D-70569, Germany

[b]Institute of Thermodynamics and Thermal Process Engineering, University of Stuttgart, Stuttgart D-70569, Germany

[c]Institute of Physical Chemistry, University of Stuttgart, Stuttgart D-70569, Germany

[d]Department of Chemistry and Center for Sustainable Systems Design (CSSD), University of Paderborn, Paderborn D-33098, Germany

Corresponding authors: michael.buchmeiser@ipoc.uni-stuttgart.de
felix.richard.fischer@uni-paderborn.de

Table of Contents

NMR Spectra

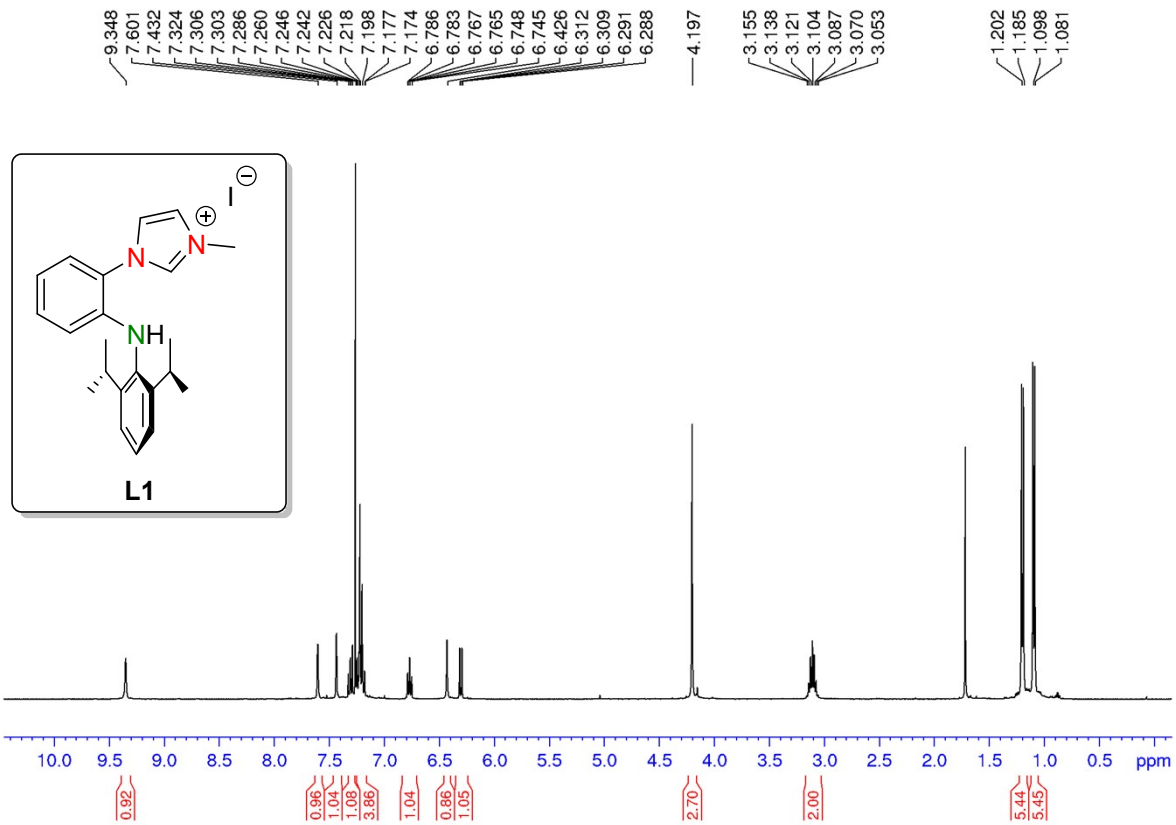

Figure S1. ^{1}H-NMR spectrum (400 MHz, $CDCl_3$) of **L1**.

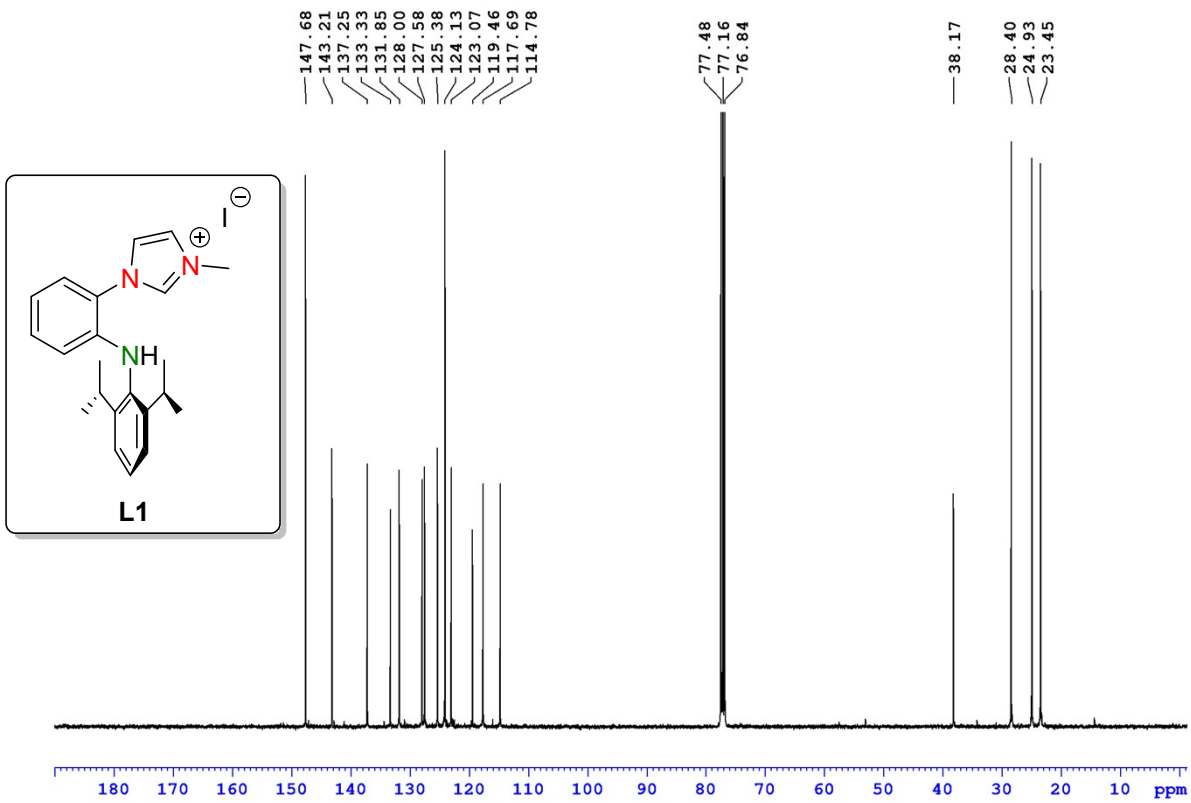

Figure S2. ^{13}C-NMR spectrum (125 MHz, $CDCl_3$) of **L1**.

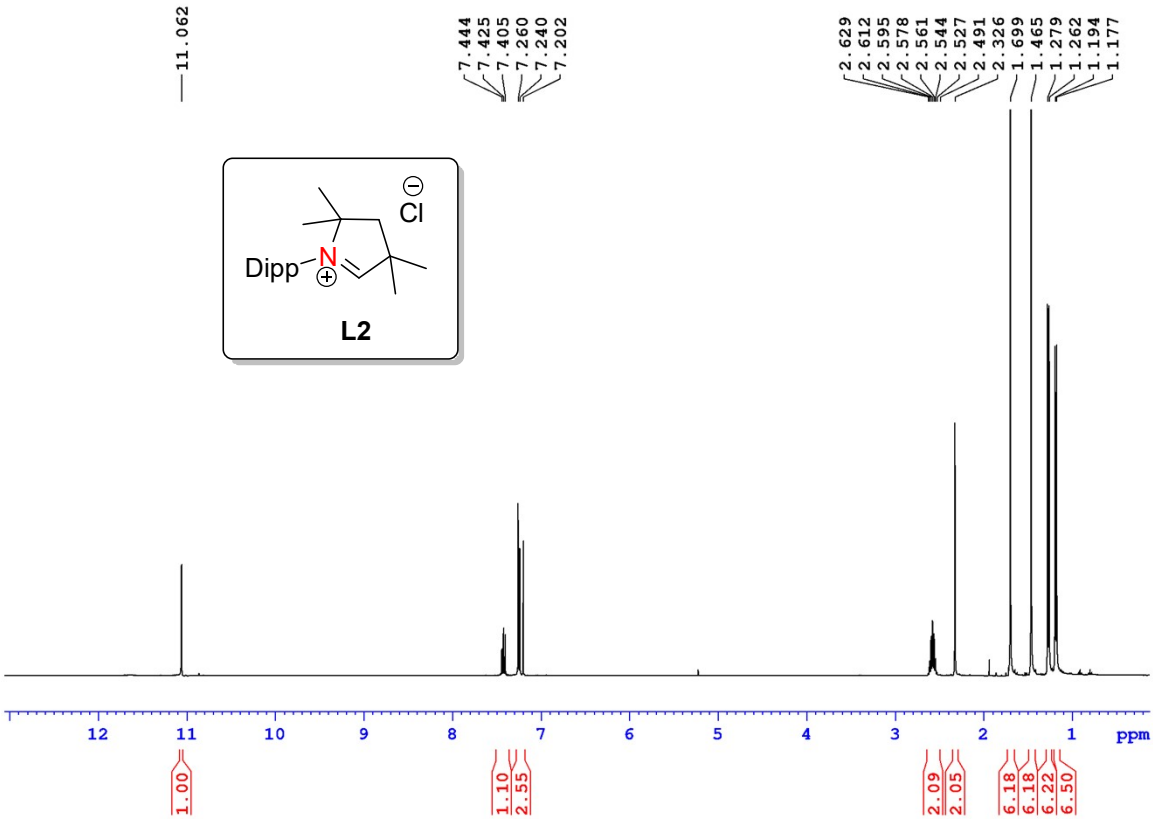

Figure S3. ^{1}H-NMR spectrum (700 MHz, $CDCl_3$) of **L2**.

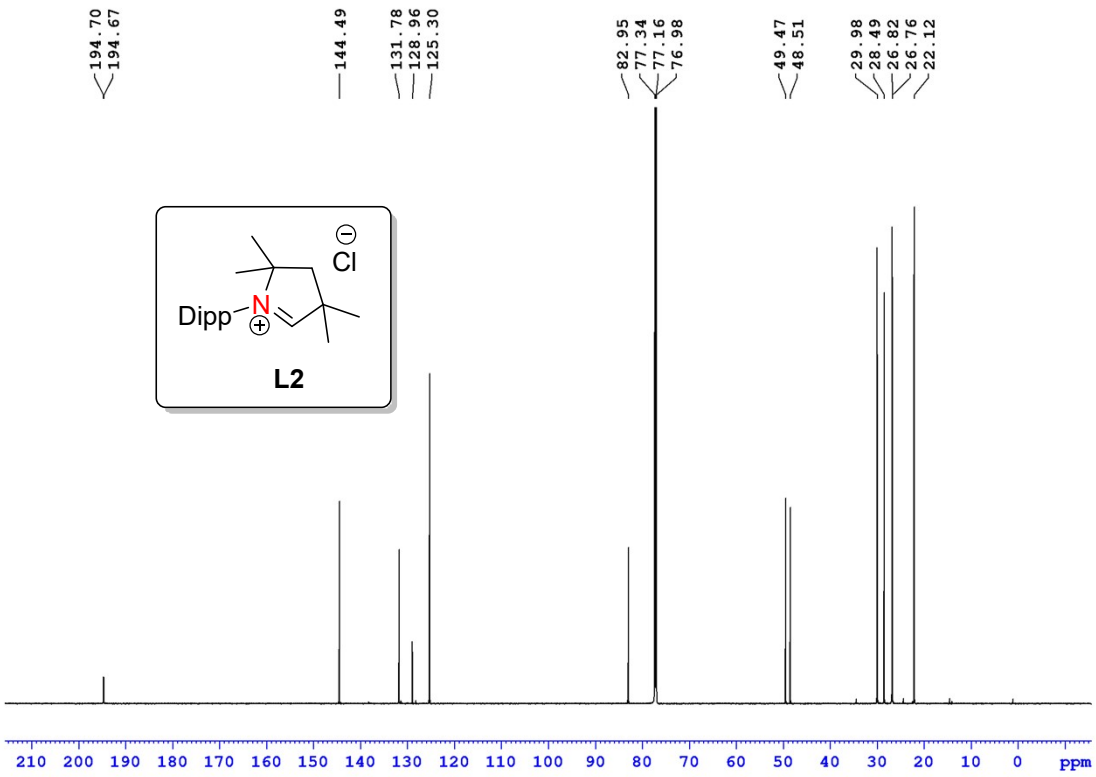

Figure S4. ^{13}C-NMR spectrum (175 MHz, $CDCl_3$) of **L2**.

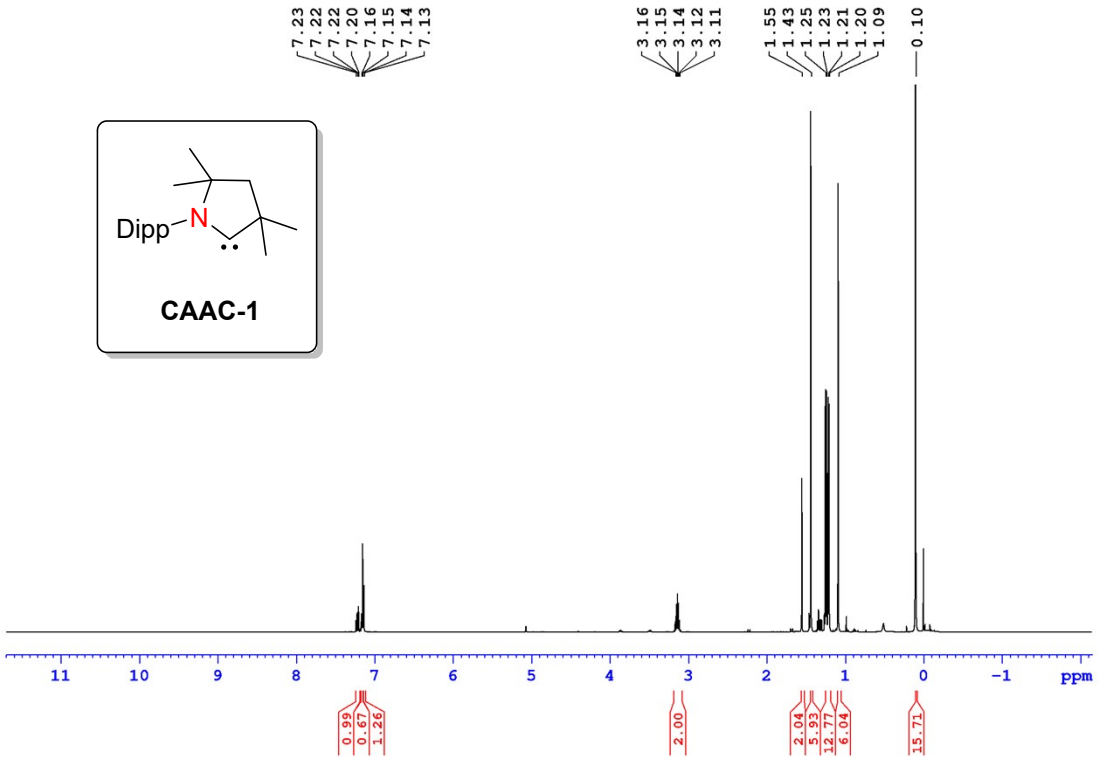

Figure S5. ^{1}H-NMR spectrum (400 MHz, C_6D_6) of **CAAC-1** (used *in situ*, the singlet at δ = 0.1 ppm indicates the presence of 0.9 equiv. of HMDS as an impurity).

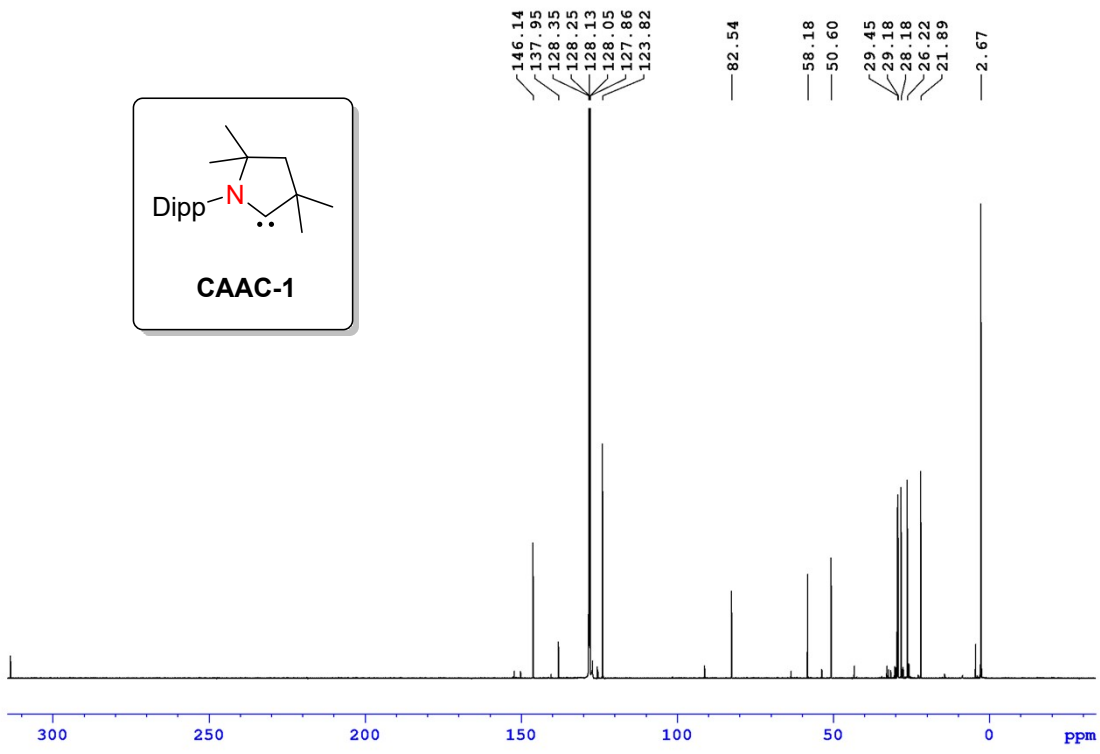

Figure S6. ^{13}C-NMR spectrum (125 MHz, C_6D_6) of **CAAC-1** (used *in situ*, the peak at δ = 2.67 ppm indicates the presence of HMDS as an impurity).

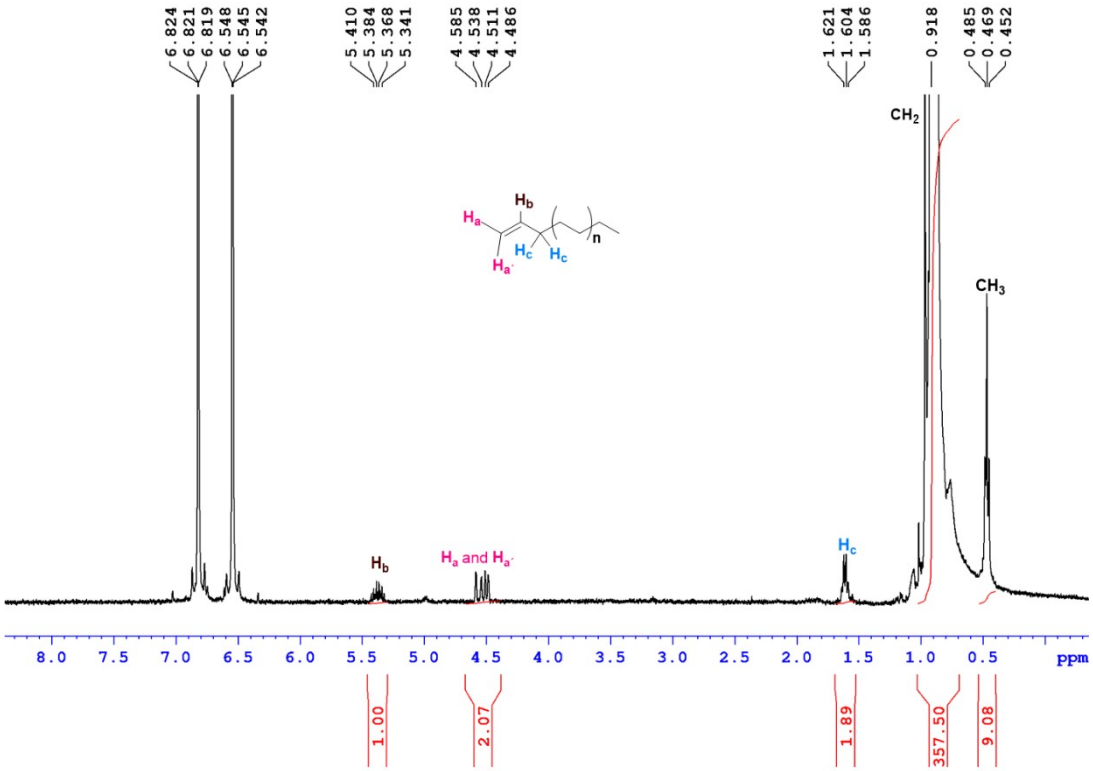

Figure S7. ^{1}H-NMR spectrum (400 MHz, 1,2-dichlorobenzene-d_4, T = 120 °C) of a PE sample obtained by the action of **Cr1@Si60/MAO**.

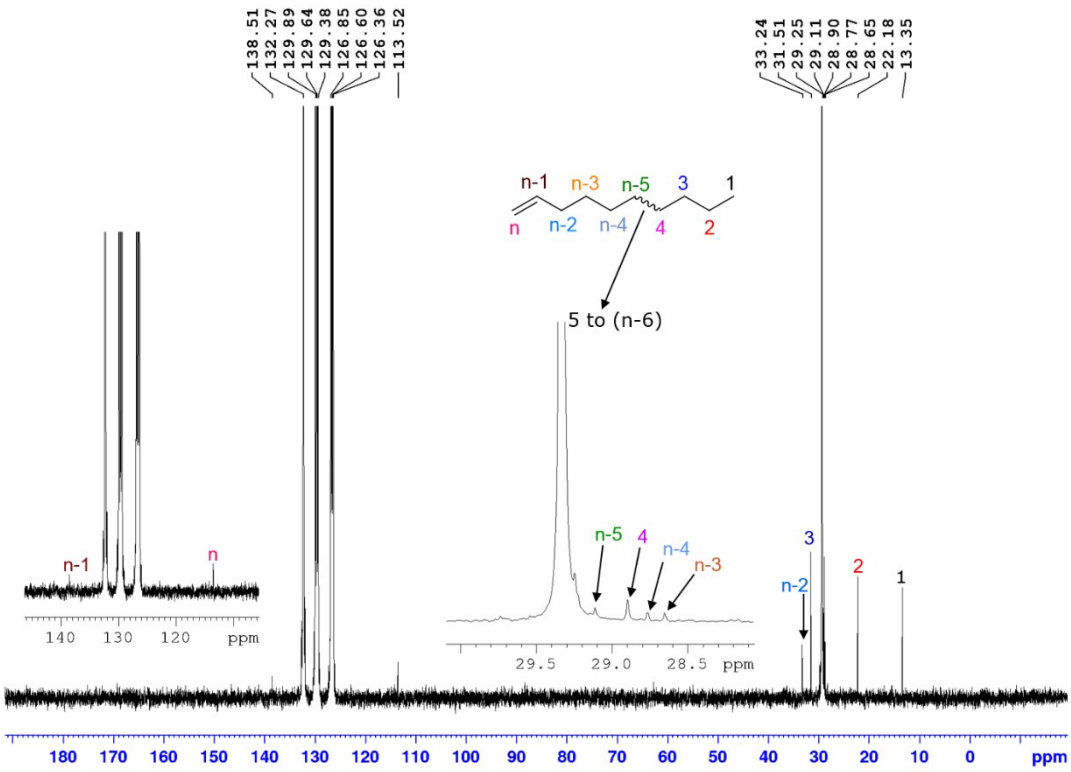

Figure S8. ^{13}C-NMR spectrum (100 MHz, 1,2-dichlorobenzene-d_4, T = 120 °C) of a PE sample obtained by the action of **Cr1@Si60/MAO**.

ICP-OES Measurements

entry	catalyst	Cr loading [µmol/g]	
		Method a[a]	Method b[b]
1	**Cr1@OMS$_{28Å}$**	52	50
2	**Cr2@OMS$_{28Å}$**	59	n.d.
3	**Cr3@OMS$_{28Å}$**	71	34
4	**Cr1@OMS$_{66Å}$**	162	n.d.
5	**Cr2@OMS$_{57Å}$**	178	n.d.
6	**Cr3@OMS$_{28Å}$**	162	n.d.
7	**Cr1@Si60**	245	n.d.
8	**Cr2@Si60**	195	n.d.
9	**Cr3@Si60**	240	172

Table S1. Determination of the Cr-content in the supported catalysts by ICP-OES.

[a] 15 mg of **Cr** cat per 100 mg of silica, 3 mL toluene, room temperature, 16 h. [b] 15 mg of **Cr** cat per 100 mg of silica, 3 mL toluene, room temperature, 4 h.

Nitrogen Physisorption Measurements

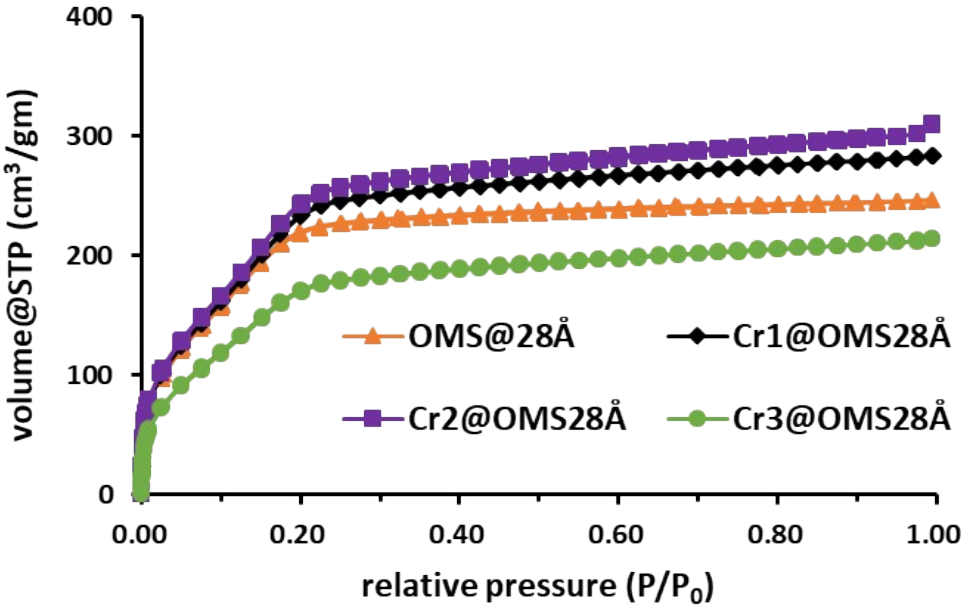

Figure S9. N_2-sorption isotherms of **$OMS_{28Å}$**, **$Cr1@OMS_{28Å}$**, **$Cr2@OMS_{28Å}$** and **$Cr3@OMS_{28Å}$**.

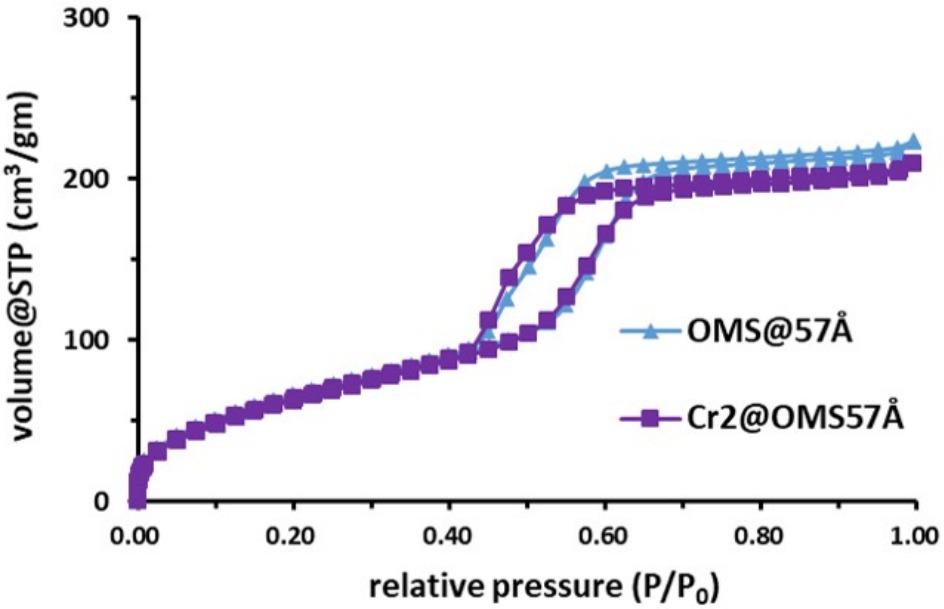

Figure S10. N_2-sorption isotherms of **$OMS_{57Å}$** and **$Cr2@OMS_{57Å}$**.

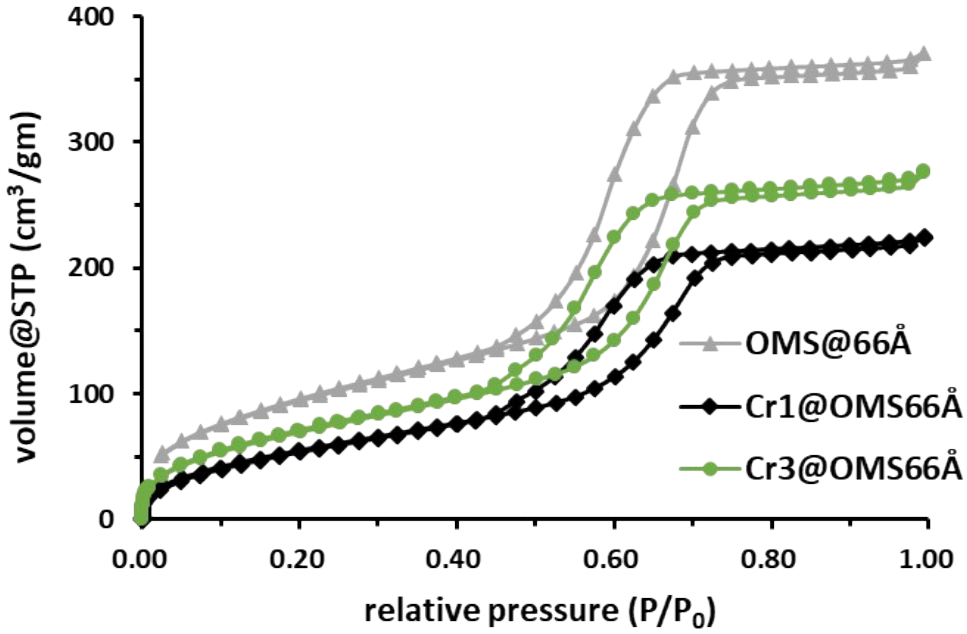

Figure S11. N_2-sorption isotherms of **$OMS_{66Å}$**, **Cr1@$OMS_{66Å}$** and **Cr3@$OMS_{66Å}$**.

XAS Measurements

Table S2. Edge energies for the immobilized compounds **Cr1@OMS$_{66Å}$**, **Cr2@OMS$_{57Å}$**, **Cr3@OMS$_{66Å}$** and the activated species **Cr3_MAO activated** compared to their homogeneous analogues (**Cr1**, **Cr2**, **Cr3**), **Cr(0)(C$_6$H$_6$)$_2$** and for a **Cr(0) foil** used as reference.

sample	edge energy E_0 [eV]
Cr1@OMS$_{66Å}$	6000.7
Cr1	5997.7
Cr2@OMS$_{57Å}$	6001.3
Cr2	5998.6
Cr3@OMS$_{66Å}$	6001.3
Cr3	5998.1
Cr3_MAO activated	5997.5
Cr(0)(C$_6$H$_6$)$_2$	5998.0
Cr(0) foil	5989.0

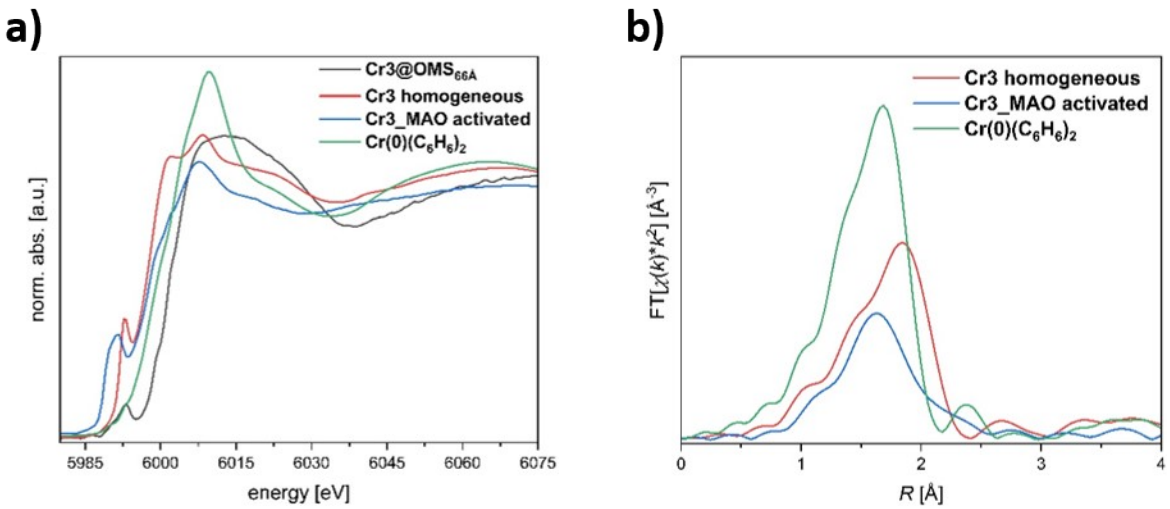

Figure S12. a) XANES spectra of **Cr3** (red), **Cr3_MAO activated** (blue) and Cr(0)(C$_6$H$_6$)$_2$ (green). b) Comparison of the FT–EXAFS spectra of **Cr3** (red), **Cr3_MAO activated** (blue) and Cr(0)(C$_6$H$_6$)$_2$ (green).

EXAFS Analysis

The *k*- and *R*-ranges of the EXAFS-analysis of complexes **Cr1@OMS$_{66Å}$**, **Cr2**, **Cr2@OMS$_{57Å}$**, **Cr3@OMS$_{66Å}$** and **Cr3_MAO activated** together with the respective values for *R*-factor, reduced Chi-square and S_0^2-parameter are summarized in Table S3. For **Cr1** and **Cr3**, the *k*-ranges to calculate the experimental FT-functions were chosen to be *k* = 1.1 – 12.2 and *k* = 2.4 – 12.7, respectively.

Figures S13 and S14 illustrate the fitted function, experimental data, residual plot as well as first shell contributions for **Cr1@OMS$_{66Å}$**, **Cr2@OMS$_{57Å}$**, **Cr2**, **Cr3@OMS$_{66Å}$** and **Cr3_MAO activated** in the *R*- and *k*-space, respectively. Table S4 shows coordination numbers (*N*), bond lengths ($R + \Delta R$) and Debye-Waller factors (σ^2) for all scattering paths of **Cr1@OMS$_{66Å}$**, **Cr2@OMS$_{57Å}$**, **Cr2**, **Cr3@OMS$_{66Å}$** and **Cr3_MAO activated** obtained by EXAFS fitting with the Artemis program.

Table S3. *k*- and *R*-ranges as well as corresponding fit parameters of the analysis of the complexes **Cr1@OMS$_{66Å}$**, **Cr2@OMS$_{57Å}$**, **Cr2**, **Cr3@OMS$_{66Å}$** and **Cr3_MAO activated**.

sample	*k*-range [Å^{-1}]	*R*-range [Å]	*R*-factor	reduced Chi-square	S_0^2-value	delE_0
Cr1@OMS$_{66Å}$	1.0 – 11.5	1.20 – 4.05	0.0005	2	1.0	-4.45(88)
Cr2@OMS$_{57Å}$	1.1 – 12.5	1.00 – 4.00	0.0004	3	1.0	-3.84(37)
Cr2	1.1 – 12.3	1.00 – 4.00	0.0015	26	1.0	-1.75(64)
Cr3@OMS$_{66Å}$	2.0 – 11.6	1.05 – 4.00	0.0033	6	1.0	-3.22(123)
Cr3_MAO activated	1.8 – 10.9	1.20 – 4.00	0.0007	19	1.0	-5.70(200)

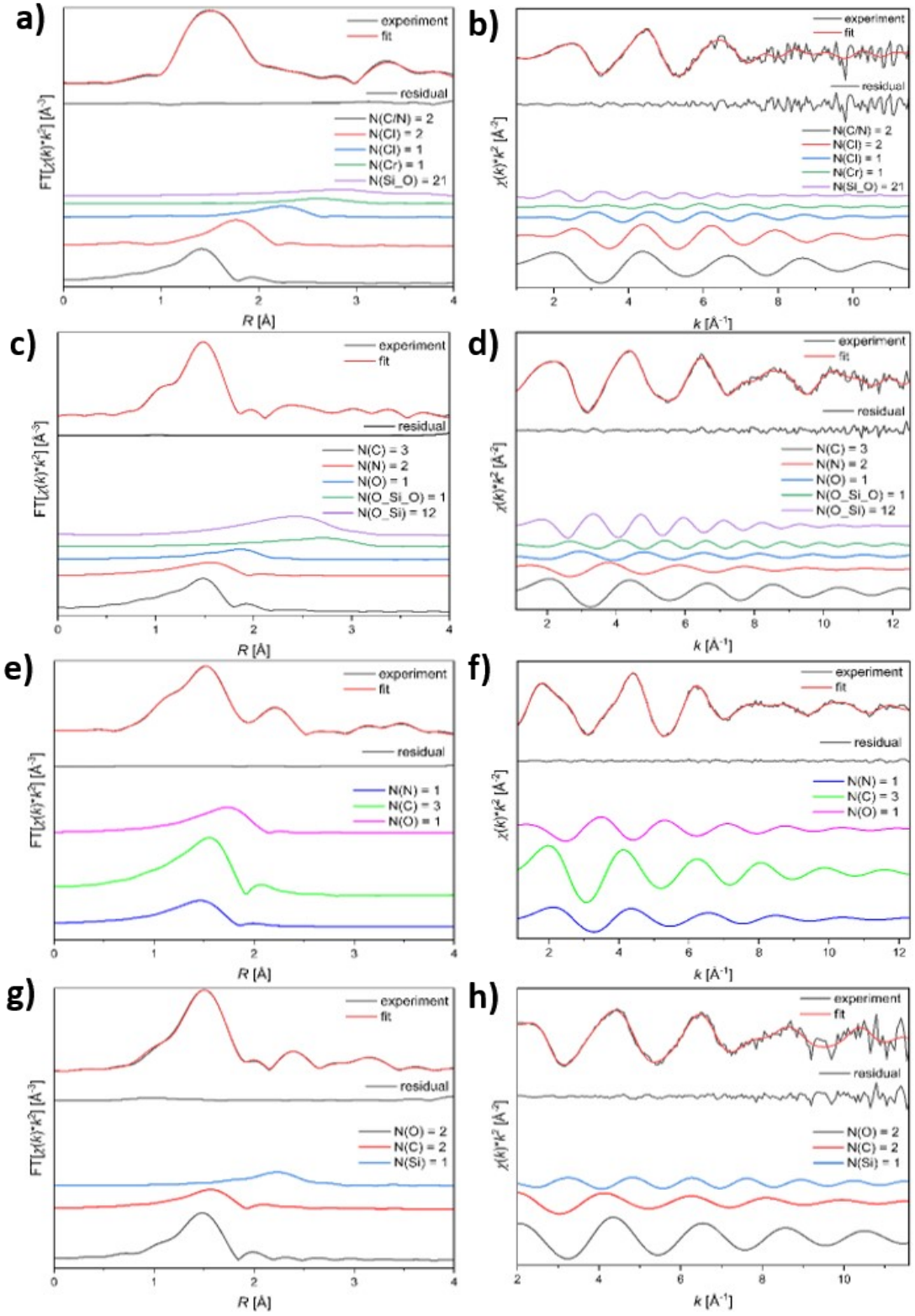

Figure S13. Fitted function compared with experimental data, residual plot and first coordination shell paths for **Cr1@OMS$_{66Å}$**, **Cr2@OMS$_{57Å}$**, **Cr2**, and **Cr3@OMS$_{66Å}$** in the *k*- and *R*-space: a) *R*-space of **Cr1@OMS$_{66Å}$**, b) *k*-space of **Cr1@OMS$_{66Å}$**, c) *R*-space of **Cr2@OMS$_{57Å}$**, d) *k*-space of **Cr2@OMS$_{57Å}$**, e) *R*-space of **Cr2**, f) *k*-space of **Cr2**, g) *R*-space of **Cr3@OMS$_{66Å}$**, h) *k*-space of **Cr3@OMS$_{66Å}$**.

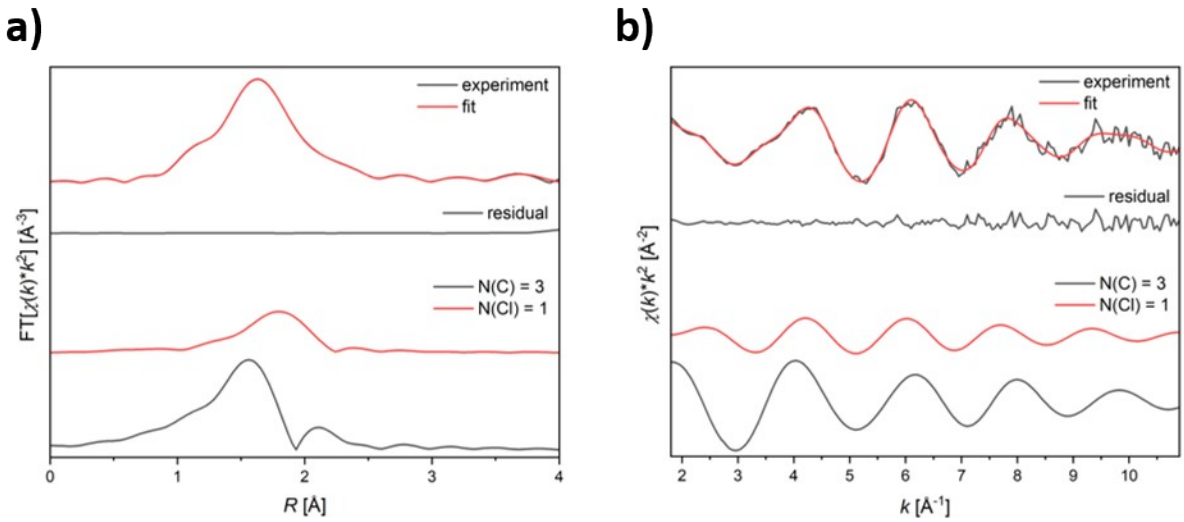

Figure S14. Fitted function compared with experimental data, residual plot and first coordination shell paths for **Cr3_MAO activated** in the *k*- and *R*-space: a) *R*-space of **Cr3_MAO activated**, b) *k*-space of **Cr3_MAO activated**.

Table S4. Coordination numbers (*N*), bond lengths ($R + \Delta R$) and Debye-Waller factors (σ^2) for all scattering paths of **Cr1@OMS$_{66Å}$**, **Cr2@OMS$_{57Å}$**, **Cr2**, **Cr3@OMS$_{66Å}$** and **Cr3_MAO activated** obtained by EXAFS fitting with the Artemis program. Cr–CC-, Cr–CN-, Cr–NC-, Cr–Cr^{2}Cl^2-, Cr–Cl^{2}C-, Cr–CCC- and Cr–SiO-scattering paths represent multiple scattering phenomena.

scattering paths	**Cr1@OMS$_{66Å}$**		
	N	$R + \Delta R$ [Å]	σ^2 [Å^2]
Cr–N	2.3(1)	1.947(7)	0.0029(4)
Cr–Cl	1.7(1)	2.247(9)	0.0082(5)
Cr–Cl	1.4(1)	2.782(15)	0.0089(6)
Cr–N	2.1(2)	2.892(23)	0.0043(6)
Cr–Cr	0.9(1)	3.134(53)	0.0106(41)
Cr–C	5.4(2)	4.916(42)	0.0058(29)
Cr–CN	5.4(4)	3.158(44)	0.0048(16)
Cr–CC	12.7(8)	3.844(58)	0.0051(26)
Cr–CCC	15.0(7)	3.979(31)	0.0046(24)
Cr-SiO	26.0(19)	3.977(85)	0.0115(8)
scattering paths	**Cr2@OMS$_{57Å}$**		
	N	$R + \Delta R$ [Å]	σ^2 [Å^2]
Cr–C	2.8(1)	2.003(3)	0.0020(3)
Cr–N	1.7(1)	2.149(11)	0.0077(13)
Cr–O	1.1(1)	2.409(10)	0.0024(14)
Cr–C	2.7(1)	2.651(7)	0.0029(5)
Cr–C	3.7(1)	2.899(5)	0.0030(5)
Cr–C	3.0(2)	3.572(10)	0.0035(5)
Cr–O	2.0(1)	3.795(6)	0.0041(14)

Cr–C	6.4(3)	3.379(7)	0.0038(6)
Cr–OSiO	1.0(1)	3.335(10)	0.0040(26)
Cr–OSi	12.4(5)	3.276(4)	0.0109(11)
Cr–CC	4.0(2)	4.877(15)	0.0055(14)
scattering paths	**Cr2**		
	N	$R + \Delta R$ [Å]	σ^2 [Å^2]
Cr-C	1.0(1)	1.997(16)	0.0070(33)
Cr-N	2.9(1)	2.109(17)	0.0061(4)
Cr-O	1.2(1)	2.277(15)	0.0070(10)
Cr-C	5.5(3)	2.622(7)	0.0085(8)
Cr-C	2.4(4)	2.865(23)	0.0095(9)
Cr-C	4.0(3)	3.089(15)	0.0098(10)
Cr-C	8.5(10)	3.702(18)	0.0119(10)
Cr-CN	13.8(16)	3.731(29)	0.0135(39)
Cr-NC	18.4(21)	3.880(21)	0.0122(26)
Cr-CO	20.7(12)	4.101(26)	0.0133(22)
scattering paths	**Cr3@OMS$_{66Å}$**		
	N	$R + \Delta R$ [Å]	σ^2 [Å^2]
Cr–O	1.9(1)	1.950(7)	0.0022(12)
Cr–C	1.7(1)	2.090(34)	0.0049(12)
Cr–Si	0.9(1)	2.781(10)	0.0035(13)
Cr–N	2.1(3)	3.231(18)	0.0037(28)
Cr–C	6.1(7)	3.462(21)	0.0071(17)
Cr–C	7.6(15)	3.751(21)	0.0079(20)
Cr–C	1.9(16)	4.063(99)	0.0083(21)
Cr–C	3.8(11)	4.346(49)	0.0099(24)
scattering paths	**Cr3_MAO activated**		
	N	$R + \Delta R$ [Å]	σ^2 [Å^2]
Cr–C	3.0(1)	2.108(15)	0.0044(11)
Cr–Cl	0.7(1)	2.338(24)	0.0067(21)
Cr–C	3.8(6)	3.119(34)	0.0065(16)
Cr–C	1.2(3)	3.196(84)	0.0067(17)
Cr–C	5.4(8)	3.904(34)	0.0082(20)
Cr–C	2.8(7)	3.960(51)	0.0083(21)
Cr–C	3.7(5)	4.357(50)	0.0091(23)
Cr–NC	8.3(4)	3,257(20)	0.0125(56)
Cr–CC	5.4(8)	4.428(44)	0.0091(23)

GC-MS Spectra

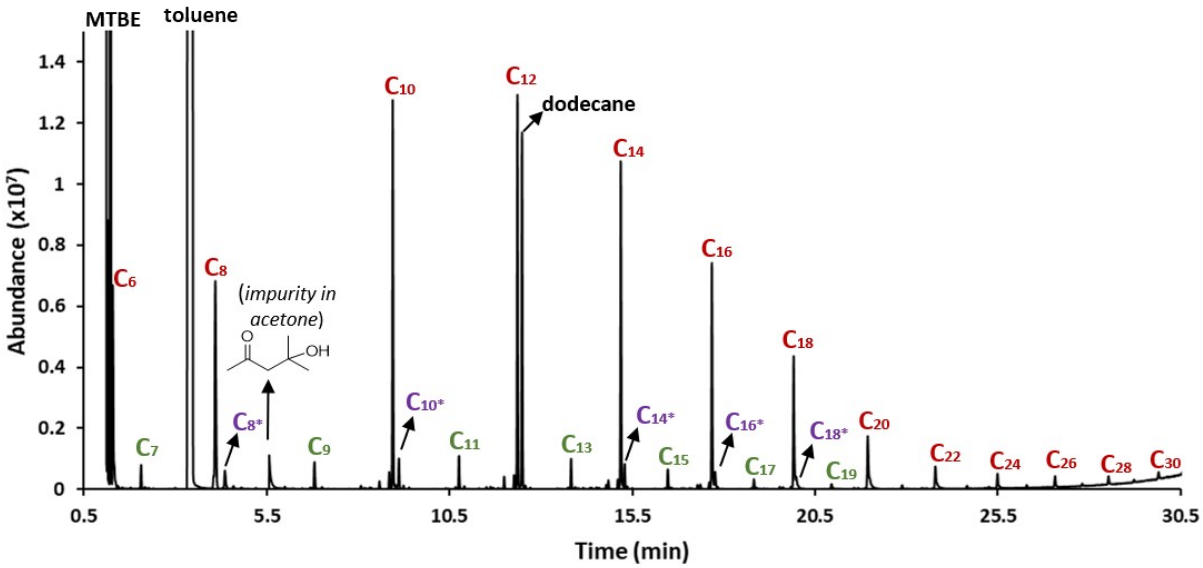

Figure S15. GC-MS spectrum of the products of a catalytic oligomerization reaction using **Cr1**/**MAO** in toluene (listed in Table 2, entry 1).

Table S5. Retention times of even and odd numbered oligomeric *n*-alkenes (C_6–C_{28}) and even numbered *n*-alkanes (C_{6*}–C_{18*}) formed using **Cr1**/**MAO** in toluene at T = 80°C and 10 bar ethylene pressure.

Oligomerization product	Retention Time
C_6	1.29
C_{6*}	1.33
C_7	2.07
C_8	4.09
C_{8*}	4.37
C_9	6.81
C_{10}	8.95
C_{10*}	9.12
C_{11}	10.76
C_{12}	12.35
C_{12*}	12.48
C_{13}	13.82
C_{14}	15.18
C_{14*}	15.28
C_{15}	16.47
C_{16}	17.68
C_{16*}	17.76
C_{17}	18.82
C_{18}	19.91
C_{18*}	19.97
C_{19}	20.94
C_{20}	21.94
C_{21}	22.94
C_{22}	23.78
C_{24}	25.49
C_{26}	27.06
C_{28}	28.52

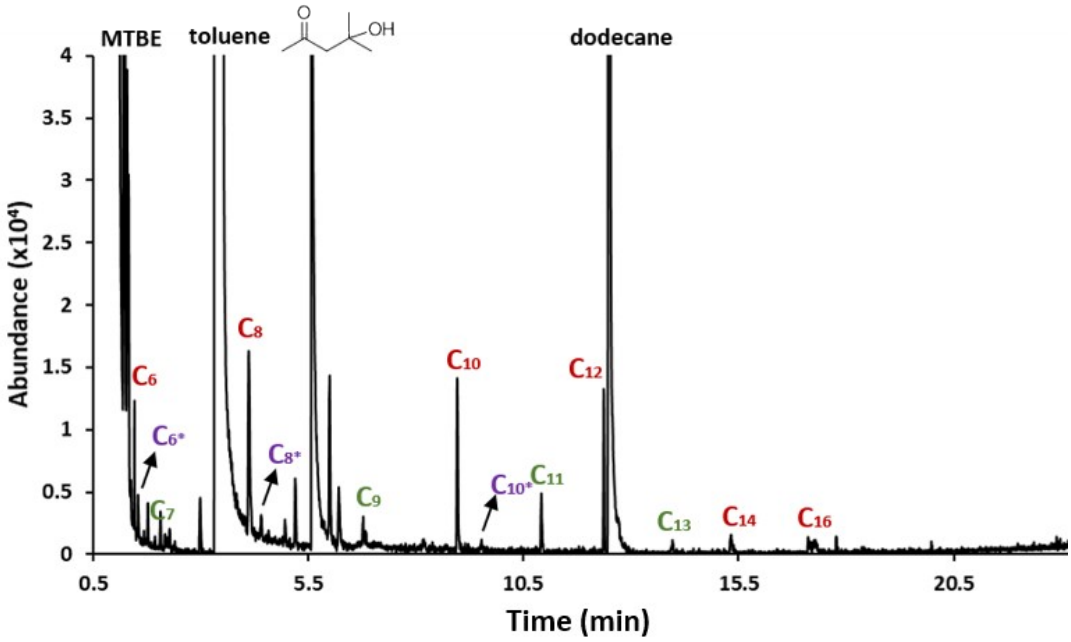

Figure S16. GC-MS spectrum of the products of a catalytic oligomerization reaction using **Cr1@OMS$_{28Å}$/MAO** in toluene (listed in Table 3, entry 4)

Table S6. Retention times of even and odd numbered oligomeric *n*-alkenes (C_6–C_{14}) and even numbered *n*-alkanes (C_{6*}–C_{12*}) formed using **Cr1@OMS$_{28Å}$/MAO** in toluene at T = 80°C and 10 bar ethylene pressure.

Oligomerization product	Retention Time
C_6	1.29
C_{6*}	1.33
C_7	2.07
C_8	4.09
C_{8*}	4.37
C_9	6.81
C_{10}	8.95
C_{10*}	9.12
C_{11}	10.76
C_{12}	12.35
C_{12*}	12.48
C_{13}	13.82
C_{14}	15.18
C_{16}	17.68

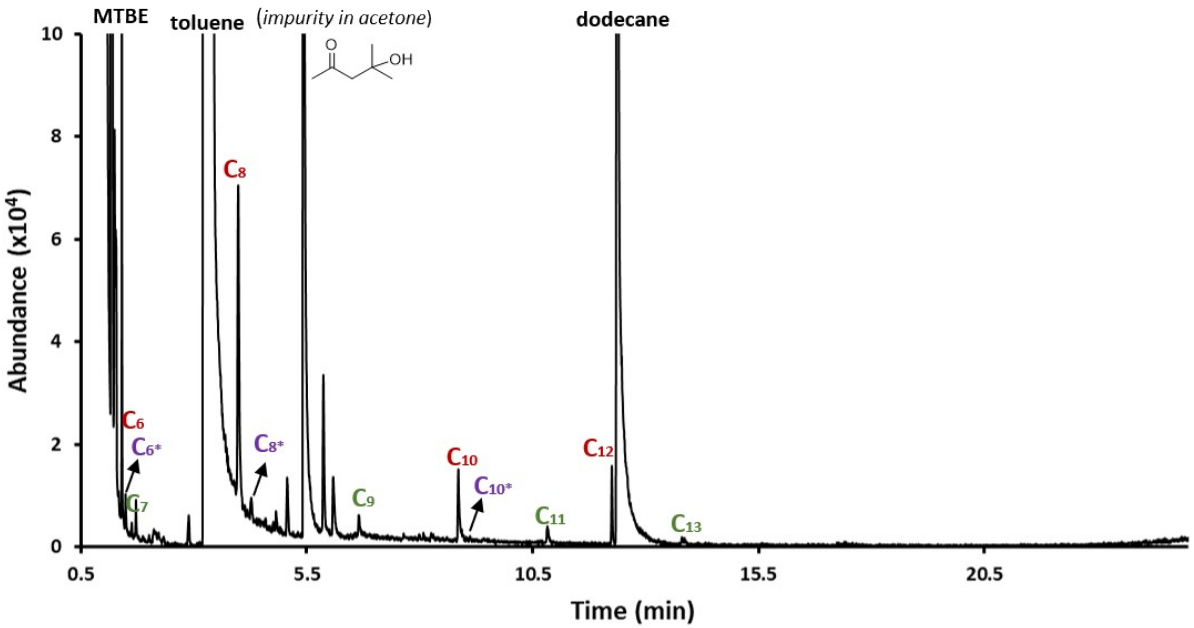

Figure S17. GC-MS spectrum of the products of a catalytic oligomerization reaction using **Cr1@OMS$_{28Å}$/MAO** in toluene (listed in Table 3, entry 5).

Table S7. Retention times of even and odd numbered oligomeric *n*-alkenes (C_6–C_{12}) and even numbered *n*-alkanes (C_{6*}–C_{12*}) formed using **Cr1@OMS$_{28Å}$/MAO** in toluene at T = 50°C and 10 bar ethylene pressure.

Oligomerization product	Retention Time
C_6	1.29
C_{6*}	1.33
C_7	2.07
C_8	4.09
C_{8*}	4.37
C_9	6.81
C_{10}	8.95
C_{10*}	9.12
C_{11}	10.76
C_{12}	12.35
C_{12*}	12.48
C_{13}	13.82

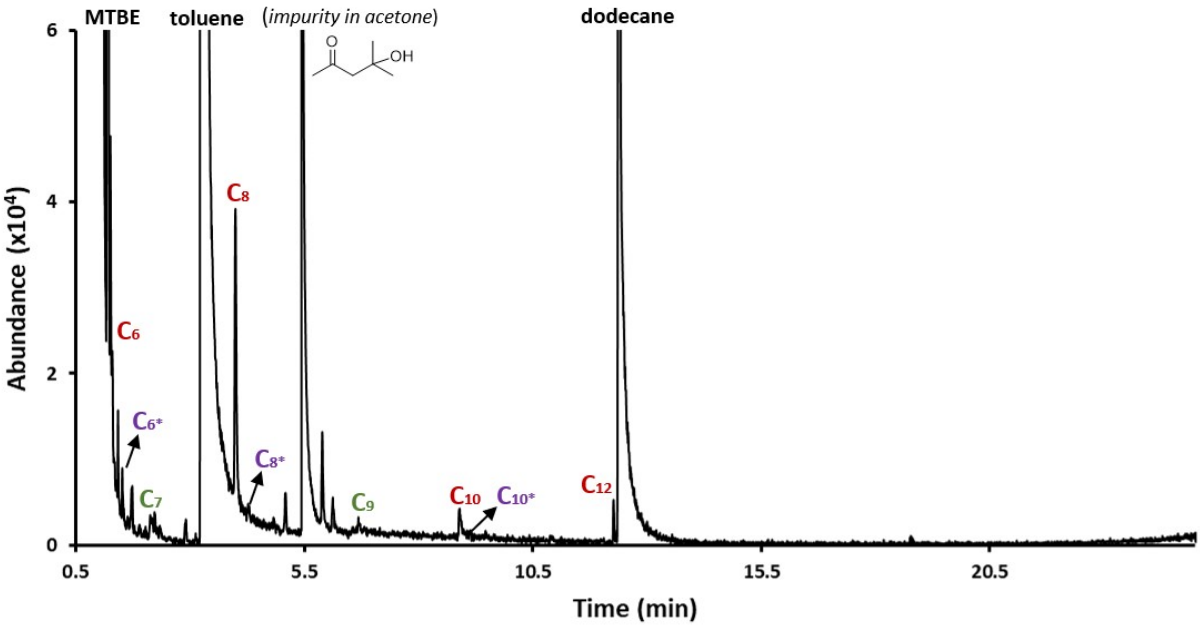

Figure S18. GC-MS spectrum of the products of a catalytic oligomerization reaction using **Cr**/**MAO** in toluene (listed in Table 3, entry 6).

Table S8. Retention times of even and odd numbered oligomeric *n*-alkenes (C_6–C_{12}) and even numbered *n*-alkanes (C_{6*}–C_{12*}) formed using **Cr1@OMS$_{28Å}$/MAO** in toluene at T = 20°C and 10 bar ethylene pressure.

Oligomerization product	Retention Time
C_6	1.29
C_{6*}	1.33
C_7	2.07
C_8	4.09
C_{8*}	4.37
C_9	6.81
C_{10}	8.95
C_{10*}	9.12
C_{11}	10.76
C_{12}	12.35
C_{12*}	12.48

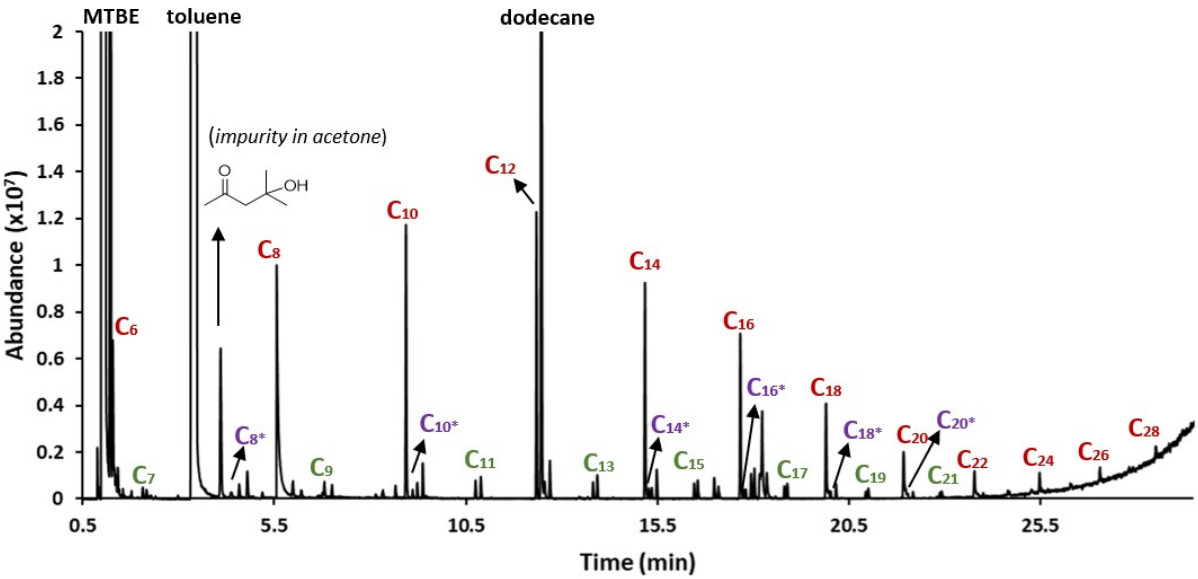

Figure S19. GC-MS spectrum of the products of a catalytic oligomerization reaction using **Cr2**/**MAO** in toluene (listed in table 2, entry 7).

Table S9. Retention times of even and odd numbered oligomeric *n*-alkenes (C_6–C_{28}) and even numbered *n*-alkanes (C_{6*}–C_{18*}) formed using **Cr2**/**MAO** in toluene at T = 80°C and 10 bar ethylene pressure.

Oligomerization product	Retention Time
C_6	1.29
C_{6*}	1.33
C_7	2.07
C_8	4.09
C_{8*}	4.37
C_9	6.81
C_{10}	8.95
C_{10*}	9.12
C_{11}	10.76
C_{12}	12.35
C_{12*}	12.48
C_{13}	13.82
C_{14}	15.18
C_{14*}	15.28
C_{15}	16.47
C_{16}	17.68
C_{16*}	17.76
C_{17}	18.82
C_{18}	19.91
C_{18*}	19.97
C_{19}	20.94
C_{20}	21.94
C_{21}	22.94
C_{22}	23.78
C_{24}	25.49
C_{26}	27.06
C_{28}	28.52

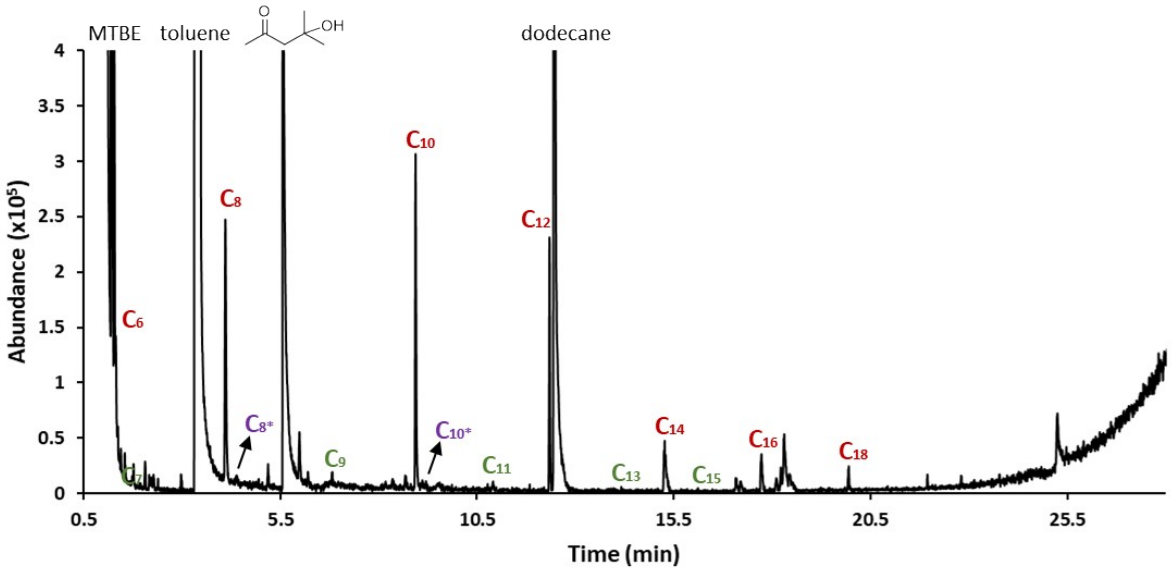

Figure S20. GC-MS spectrum of the products of a catalytic oligomerization reaction using **Cr2@OMS$_{28Å}$/MAO** in toluene (listed in Table 2, entry 10).

Table S10. Retention times of even and odd numbered oligomeric *n*-alkenes (C_6–C_{18}) and even numbered *n*-alkanes (C_{6*}–C_{14*}) formed using **Cr2@OMS$_{28Å}$/MAO** in at T = 80°C and 10 bar ethylene pressure.

Oligomerization product	Retention Time
C_6	1.29
C_{6*}	1.33
C_7	2.07
C_8	4.09
C_{8*}	4.37
C_9	6.81
C_{10}	8.95
C_{10*}	9.12
C_{11}	10.76
C_{12}	12.35
C_{12*}	12.48
C_{13}	13.82
C_{14}	15.18
C_{14*}	15.28
C_{15}	16.47
C_{16}	17.68
C_{16*}	17.76
C_{18}	19.91

DSC Measurements

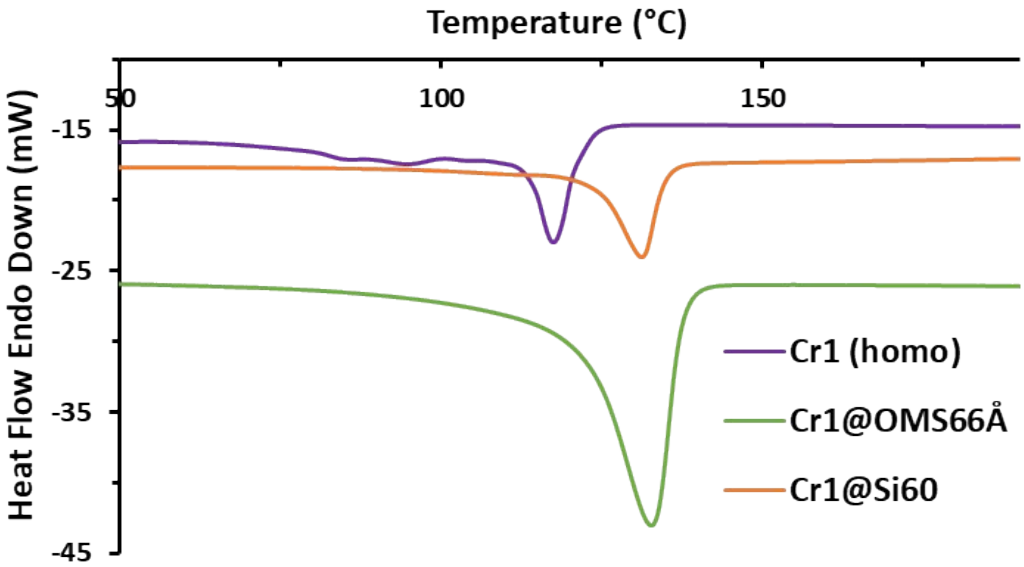

Figure S21. DSC curve (-50 °C to 200 °C, 10 °C/min, 2nd cycle) of PE obtained using **Cr1**/**MAO** (homo) (purple), **Cr1@OMS$_{66Å}$**/**MAO** (green) and **Cr1@Si60**/**MAO** (orange, listed in Table 3, entries 1-3).

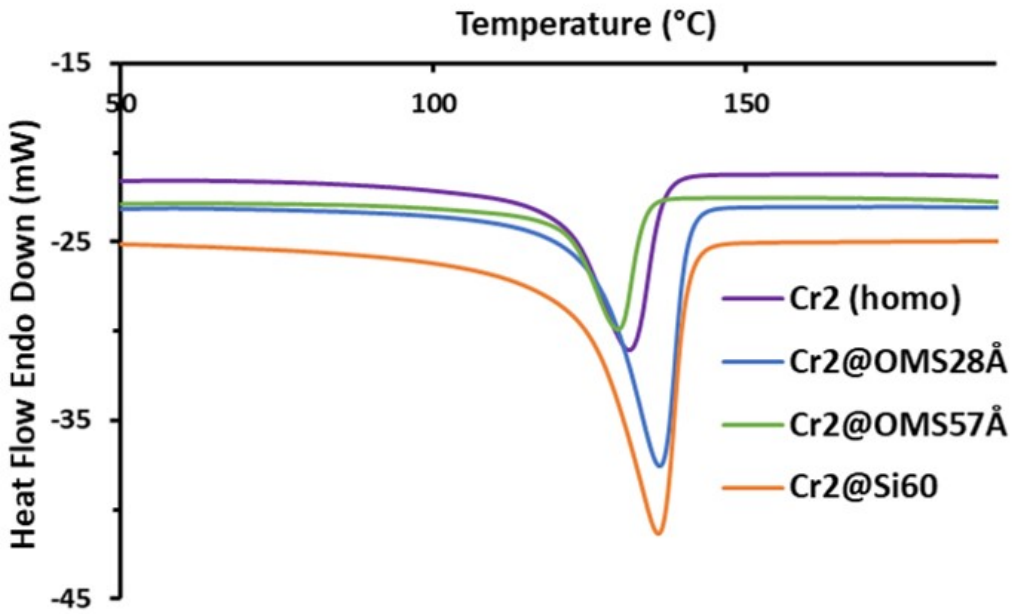

Figure S22. DSC curve (-50 °C to 200 °C, 10 °C/min, 2nd cycle) of PE obtained using **Cr2**/**MAO** (homo) (purple), **Cr2@OMS$_{28Å}$**/**MAO** (blue), **Cr1@OMS$_{66Å}$**/**MAO** (green) and **Cr1@Si60**/**MAO** (orange, listed in Table 3, entries 7-10).

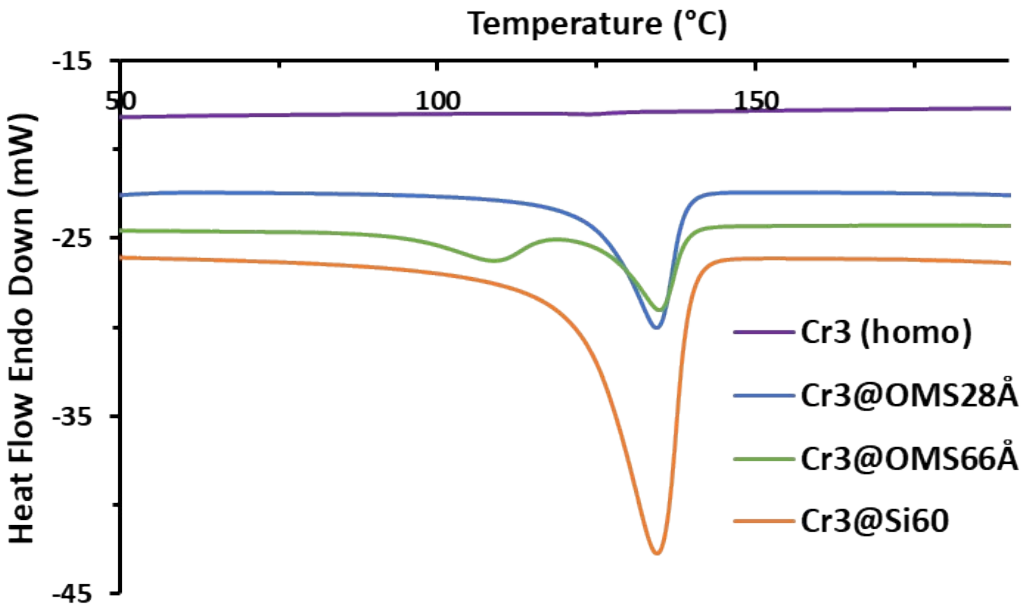

Figure S23. DSC curve (-50 °C to 200 °C, 10 °C/min, 2nd cycle) of PE obtained using **Cr3**/**MAO** (homo) (purple), **Cr3@OMS$_{28Å}$**/**MAO** (blue), **Cr3@OMS$_{66Å}$**/**MAO** (green) and **Cr3@Si60**/**MAO** (orange, listed in Table 3, entries 11-14).

Molecular Dynamics Simulations

Generation of the pore models

The Python package PoreMS[1, 2] was used to generate two cylindrical mesopore models 28 and 66 Å in diameter, respectively. These were carved through the (111)-face of a β-cristobalite silica block (80.96 x 78.93 x 107.04 Å (x · y · z)) along the z-direction. The silanol density on the inner surface was set to 3 μmol·m^{-2} and the outer surface of the silica block was functionalized with TMS molecules to prevent clustering at the pore entrance. The cylindrical pore was flanked by two solvent reservoirs.

Table S11. Pore systems with surface density.

System	Diameter / Å	Hydroxylation of inner surface / (μmol·m^{-2})
βCR−28	28	2.99
βCR−66	66	3.00

Force field

The Lennard-Jones parameters for the silica lattice and silanol groups were adopted from Coasne and Fourkas[3]. Partial atomic charges were taken from Gulmen and Thompson[4] consistent with previous studies[5]. These parameters are summarized in Table S12. For the TMS surface groups, the solvent and the alkenes, the GAFF force field was employed.[6] The alkene initial structures were generated using RDKIT[7], and Ambertools[8] was used for the force field generation.

Table S12. Lennard-Jones parameter and partial atomic charges of the silica atoms (Si, O_{Si}) in the pore grid and of the silanol groups (SI,O,H) on the pore surface.

Atom	$\sigma(nm)$	$\epsilon(kJmol^{-1})$	$q(\lvert e\rvert)$
Si	0.4550	0.1678693	1.28
O_{Si}	0.3210	0.9573535	-0.64
O_H	0.3210	0.9573535	-0.74
H	0.2750	0.1121899	0.42

Topologies in GROMACS format, input files and final configurations can be retrieved from the Data Repository of the University of Stuttgart (DaRUS) under https://doi.org/10.18419/DARUS-5511.

Simulation details

All MD simulations were carried out using the GROMACS 2019.6 program package[9] as described previously[10]. The preprocessing of the simulations was conducted with the software tool PoreSim[11]. The production run was started with no 1-alkenes present

in the pore area for all simulations. The number of C-atoms in all simulations was kept constant.

Table S13. Compositions of the simulated pore systems.

System	Label	Toluene	C_{12}	C_{14}	C_{16}	C_{18}	Simulation time / ns
βCR−2.8	βCR−28-C12	5198	50	0	0	0	600
	βCR−28-C14	5203	0	43	0	0	600
	βCR−28-C16	5203	0	0	37	0	600
	βCR−28-C18	5196	0	0	0	33	600
	βCR−28-CX	5269	20	17	15	13	600
βCR−6.6	βCR−66-C12	6675	50	0	0	0	600
	βCR−66-C14	6606	0	43	0	0	600
	βCR−66-C16	6659	0	0	37	0	600
	βCR−66-C18	6674	0	0	0	33	600
	βCR−66-CX	6710	20	17	15	13	600

Additional results

In the post-processing stage, we used the *gmx select* command to determine the number of molecules in the pore area at each sampling point. Figures S24 and S25 show the probability of pore occupancy for the simulations containing only a single 1-alkene type. Comparing the results for different diameters reveals significant differences. For the small diameter, the 1-dodecene molecules enter the small pore; the 1-tetradecene molecules can also enter the pore, yet to a lesser extent compared to the larger diameter. The large 1-hexadecenes and 1-octadecenes do not enter the small pore to a significant extent. In the large pore, all 1-alkenes can enter in greater quantities.

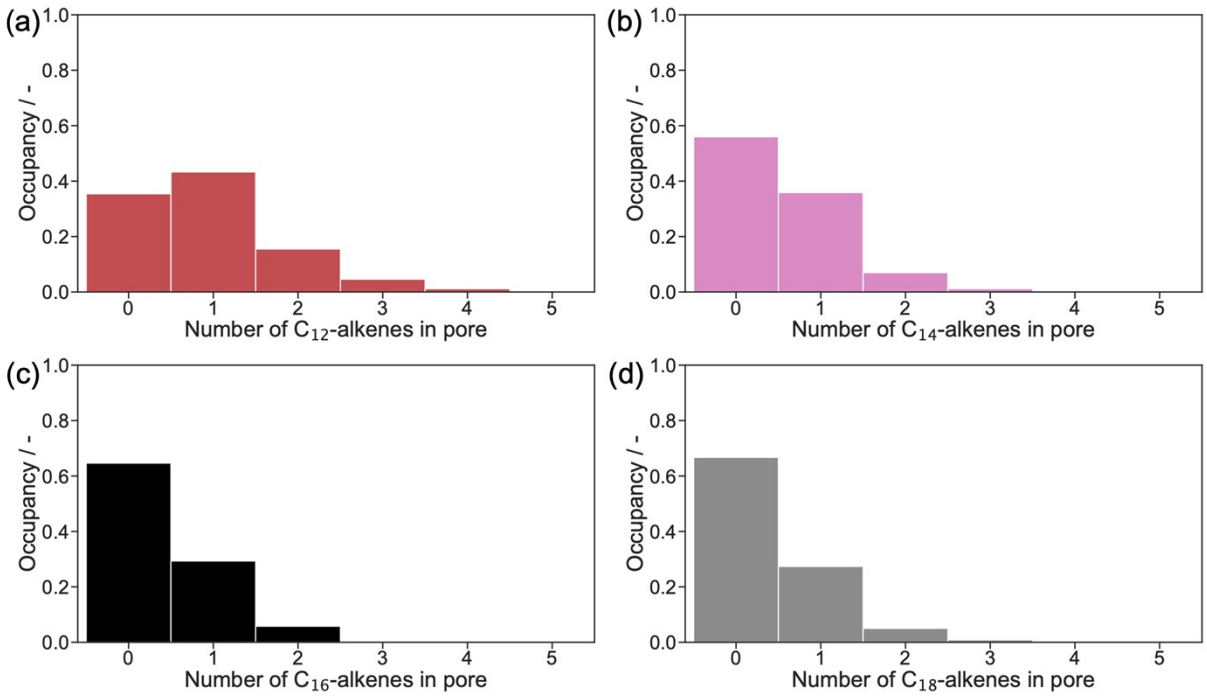

Figure S24. Frequency of occupancy of 1-alkenes in the pore for the simulations (a) *β*CR−28-C12, (b) *β*CR−28-C14, (c) *β*CR−28-C16 and (d) *β*CR−28-C18.

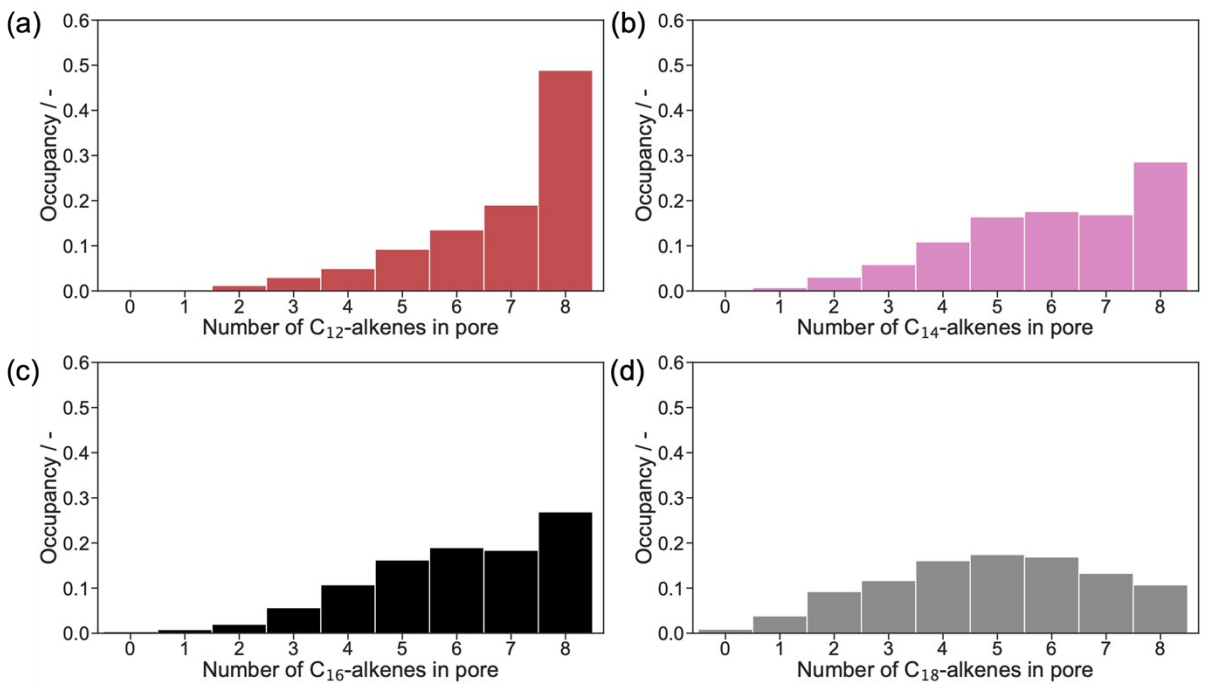

Figure S25. Frequency of occupancy of 1-alkenes in the pore for the simulations (a) *β*CR−66-C12, (b) *β*CR−66-C15, (c) *β*CR−66-C16 and (d) *β*CR−66-C18.

References

1. Kraus, H.; Rybka, J.; Höltzel, A.; Trebel, N.; Tallarek, U.; Hansen, N. PoreMS: a software tool for generating silica pore models with user-defined surface functionalisation and pore dimensions. *Mol. Simul.* **2021**, *47,* 306-316.
2. Kraus, H.; Högler, M.; Hansen, N. PoreMS: 0.3.0. **2021**, https://doi.org/10.5281/zenodo.14028652.
3. Coasne, B.; Fourkas, J. T. Structure and dynamics of benzene confined in silica nanopores. *J. Phys. Chem. C* **2011**, *115,* 15471-15479.
4. Gulmen, T. S.; Thompson, W. H. Testing a two-state model of nanoconfined liquids: Conformational equilibrium of ethylene glycol in amorphous silica pores. *Langmuir* **2006**, *22,* 10919-10923.
5. Kraus, H.; Hogler, M.; Hansen, N. Axial diffusion in liquid-saturated cylindrical silica pore models. *J. Phys. Chem. C* **2023**, *127,* 14374-14388.
6. Wang, J.; Wolf, R. M.; Caldwell, J. W.; Kollman, P. A.; Case, D. A. Development and testing of a general amber force field. *J. Comp. Chem.* **2004**, *25,* 1157-1174.
7. Landrum, G.; Tosco, P.; Kelley, B.; Rodriguez, R.; Cosgrove, D.; Vianello, R.; Sriniker, P.; Gedeck, G.; Jones, G.; Schneider, N.; Kawashima, E.; Nealschneider, D.; Dalke, A.; Swain, M.; Cole, B.; Turk, S.; Savelev, A.; Vaucher, A.; Wójcikowski, M.; Take, I.; Scalfani, V. F.; Walker, R.; Probst, D.; Ujihara, K.; Tadhurst, C.; Pahl, A.; Godin, G.; Lehtivarjo, J.; Bérenger, F.; Bisson, J. in rdkit/rdkit: 2024_09_2 (Q3 2024) https://doi.org/10.5281/zenodo.13990314. **2024**.
8. Case, D. A.; Aktulga, H. M.; Belfon, K.; Cerutti, D. S.; Cisneros, G. A.; Cruzeiro, V. W. D.; Forouzesh, N.; Giese, T. J.; Gotz, A. W.; Gohlke, H. AmberTools. *J. Chem. Inf. Model.* **2023**, *63,* 6183-6191.
9. Abraham, M. J.; Murtola, T.; Schulz, R.; Páll, S.; Smith, J. C.; Hess, B.; Lindahl, E. GROMACS: High performance molecular simulations through multi-level parallelism from laptops to supercomputers. *SoftwareX* **2015**, *1,* 19-25.
10. Nguyen, H.-H.; Högler, M.; Schnabel, N.; Hansen, N.; Sottmann, T.; Estes, D. P. Effects of Surfaces and Confinement on Formic Acid Dehydrogenation Catalyzed by an Immobilized Ru–H Complex: Insights from Molecular Simulation and Neutron Scattering. *ACS Catal.* **2024**, *14,* 11252-11261.
11. Kraus, H.; Högler, M.; Hansen, N. PoreSim: 0.2.0 (v0.2.0). Zenodo. **2024**.